Time-variant planar laser-induced fluorescence for thickness measurement of wavy liquid films: a calibration-free and threshold-free method

Kamada, Yoshiaki
Department of Aeronautics and Astronautics, Kyushu University

Wang, Zhenying
Department of Aeronautics and Astronautics, Kyushu University

Inoue, Chihiro
Department of Aeronautics and Astronautics, Kyushu University

Senoo, Shigeki
Mitsubishi Heavy Industries, Ltd.

https://hdl.handle.net/2324/7347392

出版情報：Experiments in Fluids. 66 (3), pp.58-, 2025-02-17. Springer
バージョン：

Time-variant planar laser-induced fluorescence for thickness measurement of wavy liquid films: A calibration-free and threshold-free method

Yoshiaki Kamada[1], Zhenying Wang[1], Chihiro Inoue[1],
Shigeki Senoo[2]

[1]Department of Aeronautics and Astronautics, Kyushu University,
744 Motooka, Nishi-ku, Fukuoka, 819-0395, Japan.
[2]Mitsubishi Heavy Industries, Ltd., Takasago, Hyogo, 676-8686, Japan.

Abstract

The planar laser induced fluorescence (PLIF) method has been widely applied for measuring the thickness of liquid films. To identify the liquid-gas interface, however, PLIF-based methods require an artificial threshold value of brightness or a calibration curve between the thickness and the brightness, limiting its application in measuring unknown film thickness. To overcome the drawbacks, we propose a new method, time-variant PLIF (T-PLIF), which employs an index of time-variance of brightness to detect the interface. We first establish the mathematical principle of T-PLIF, wherein the time-variance of a phase dependent variable becomes the maximum exactly at the time-averaged position of the wavy interface. We then perform experiments for a well-controlled downward annular liquid film flow to test the reliability of T-PLIF. We demonstrate that T-PLIF measures liquid film thickness of $\boldsymbol{h > 0.2}$ **mm** with the accuracy of $\boldsymbol{\varepsilon \leq 10\%}$ to the theoretical reference and $\boldsymbol{h \leq 0.2}$ **mm** with $\boldsymbol{\varepsilon = 20\%}$. T-PLIF is able to quantify the film thickness with no need for any pre/post-calibration or artificial threshold values. We further confirm the applicability of T-PLIF to the wavy film flow sheared by an airflow up to **30 m/s** by measuring the phase velocity and wavelength, which well matches the theoretical results.

Keywords: PLIF, annular flow, gravity, viscosity, gas shear, high-speed imaging

1 Introduction

Liquid film flow on a wall is an important phenomenon accompanying heat and mass transfer in various industrial processes including coating (Weinstein and Ruschak 2004), liquid film cooling (Fujii et al. 2022, Wu et al. 2023), condensation (Berto et al. 2021, Zhang et al. 2022), vapor generation (Baptistella et al. 2023), as well as in erosion issues (Fujisawa et al. 2020, Khan and Sasikumar 2022). When a high-speed gas flows over a liquid film, the shear force disturbs the liquid film, generating three-dimensional unstable waves with droplet entrainment in cases. Past studies have been devoted to understanding the sequential phenomena from three aspects - experimental visualization/measurement (Azzopardi 1997, Schubring et al. 2010, An et al. 2020), theoretical analyses (Demekhin et al. 2007, Bhat and Samanta 2019), and numerical simulation (Kharlamov et al. 2015, Bender et al. 2019). However, the complex topology of the unsteady flow imposes difficulties in accurately capturing the liquid-gas interface, making it hard to reach a quantitative understanding of the dynamics of wavy film flows. Since the film thickness is often utilized as a characteristic length scale to determine the wave structure, it is essential to develop reliable techniques for accurately capturing the interfaces and measuring the film thickness.

Non-intrusive optical methods such as X-ray tomography (Aliseda and Heindel 2021), near-infrared laser (Dupont et al 2015, Zhao et al. 2022), and ultrasound (Al-Aufi et al. 2019) have been adopted to measure film thickness from the scale of $O(10^{-5})$ m to $O(10^{-3})$ m, with high spatiotemporal resolution. These methods make it possible to analyze multiphase flow with minimal external disturbance. X-ray methods estimate the density of each phase by collecting the beam intensity before and after passage through the medium, based on the attenuation rate. In X-ray stereography, two sets of X-ray sources and detectors are usually combined to reconstruct a projection image and obtain three-dimensional information about the liquid film (Skjæraasen and Kasana 2020). However, it can only be used in limited scenarios due to safety issues. The near-infrared measurement method also makes use of changes in signal intensity when passing through the liquid phase. As a high responsive method applicable to a single point measurement, Mizushima 2023 developed a system using a reflection of laser light emitted from an optical fiber. However, these methods have trade-offs between spatial and temporal resolution, show high sensitivity to temperature variations, and require precise calibration prior to experimentation.

Experimental techniques based on Laser-Induced Fluorescence (LIF) have been widely employed (Schubring et al. 2010, Farias et al. 2012, Alekseenko et al. 2012, Charogiannis et al. 2015), which are categorized into two types as Planar Laser-Induced Fluorescence (PLIF) and Brightness-Based Laser-Induced Fluorescence (BBLIF). The PLIF method excites a two-dimensional cross-section of fluorescent dyed fluid and directly visualizes the fluorescence intensity, and has been widely used in the research of multiphase flow. In addition to visualizing liquid dynamics, PLIF has been applied for simultaneous measurement of velocity and temperature fields in liquid (Markides et al. 2016, Charogiannis et al. 2017), as well as for visualizing diffusion flames in turbulent mixing fields (Yan et al. 2022, 2023, 2024). The BBLIF method visualizes the fluorescence intensity from the liquid film with a camera arranged at the same side of the exciting laser source, allowing for measurement of the projected thickness distribution following the calibration result based on the Beer-Lambert law (Alekseenko et al. 2012, Cherdantsev et al. 2019, Chang et al. 2023). With this method, Cherdantsev et al. (2014) reconstructed the bubbles in the liquid film and the entrained droplets at the interface.

A general source of measurement error with the LIF-based method is the temperature dependency of luminescence intensity of Rhodamine B - a widely used fluorescent dye (Ross et al. 2001). When applying PLIF to annular flows, the thickness of smooth liquid films can be overestimated due to the total reflection at the gas-liquid interface (Häber et al. 2015). On the other hand, when the liquid film is strongly corrugated, light from the wave crest may not reach the camera due to light scattering, which raises the risk of underestimating both the film thickness and the wave amplitude (Cherdantsev et al. 2019). Moreover, most of the existing studies require an artificial threshold value of the brightness (Schubring et al. 2010, Farias et al. 2012, Charogiannis et al. 2015) or the brightness gradient (Zadrazil et al. 2014, Markides et al. 2016, Cherdantsev et al. 2019) to identify the liquid-gas interface. To solve this problem, researchers use image processing to reduce noise by applying a Median filter (Schubring et al. 2010), with contrast adjustment by a histogram equalization method of brightness (Farias et al. 2012), or through edge detection with suppressed reflections at the interface (Charogiannis et al. 2015). In such cases, we need to carefully select a type of filter and adjust the strength so as not to change the position of visible interface.

Due to the unavoidable error sources and practical limitations involved in the LIF-based methods, it is challenging to measure the accurate thickness of thin and blurred fluorescent liquid films. To overcome these limitations, Xue et al. (2022) suggested positioning the camera and the laser sheet at a 40-degree angle to reduce the effects of total reflection. Other researchers have also proposed methods to rectify the interface using a calibration curve based on detailed ray tracing (Xue et al. 2024, Rivera et al. 2023 2024, Jiang et al. 2024). In addition, Charogiannis et al. (2019) employed structured illumination in the PLIF setup to detect the liquid-gas interface. By combining PLIF with periodically modulated laser intensity, they eliminated the effects of reflection and refraction owing to waviness, allowing for accurate positioning of the gas-liquid interface. This technique has been reported to show deviations of less than 10 % from the average film thickness measured by capacitance probe for thin films (Voulgaropoulos et al. 2021).

To summarize, previous LIF-based methods use the value or the gradient of brightness of a snapshot or a time-averaged image to detect the interface, while the apparatus and analysis become inevitably complex for improving the accuracy. In the present paper, we propose a simple method based on clear mathematical principle. Specifically, we analyse the time-variance of brightness, enabling reliable measurement of the film thickness without any pre/post-calibration or artificial threshold value. In this paper, we introduce the new time-variance PLIF-based method (referred as T-PLIF in the following context) and experimentally validate its feasibility in the measurement of wavy liquid film thickness. Here, the experiment is conducted with well-controlled annular liquid film flow with tunable airflow, where theoretical expressions of the film thickness exist for comparison with the results by T-PLIF.

In the remainder of the paper, we introduce the experimental setup in Sec. 2, establish the principle of T-PLIF in Sec. 3, and experimentally demonstrate the validity of T-PLIF in Sec. 4. The conclusions are summarized in Sec. 5, and the supporting information provided in the Appendix.

2 Experimental setup

Figure 1(a) shows the experimental setup for producing annular liquid film flow with central gas stream toward the gravitational direction. The working fluid of water dyed by fluorescent Rhodamine B is supplied from the reservoir tank at room temperature pressurized by the compressor. The water passes through the mother tube that branches into four daughter tubes which distribute around the acrylic pipe at 90-degree intervals. The acrylic pipe has an inner diameter of $D_l = 21$ mm, a thickness of $h_t = 2$ mm, and a vertical length of 70 mm for the test section. Aligned at the center of the acrylic pipe, a stainless steel pipe is installed with an inner diameter of $D_g = 19$ mm and a total length of 500 mm for the central gas flow path. Before the experiment, we measure the weight of injected water during a certain time period to derive the flow rate with relative error of ±0.5 %. The supplied liquid initially flows through the coaxial flow path between the stainless steel pipe and the acrylic pipe at the gap

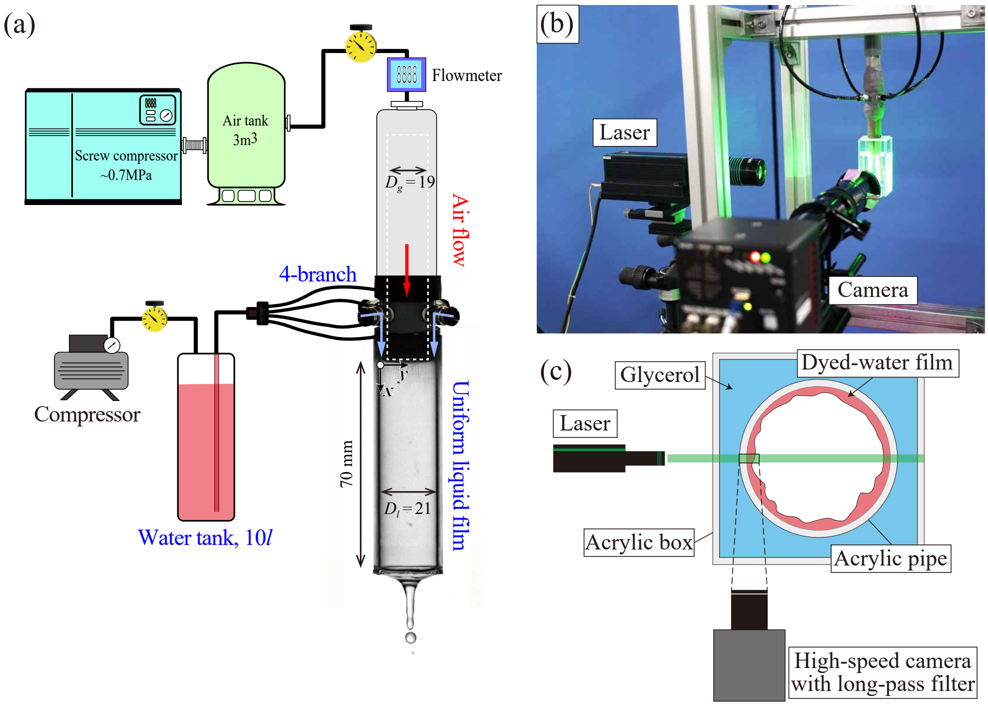

Fig. 1: Experimental setup (a) Schematic diagram. Smooth film is produced when the central airflow stops. (b) Setup of the imaging system for PLIF. (c) Top view of the PLIF system.

height of $h_0 = 0.5$ mm (corresponding to the initial film thickness), then keep flowing on the acrylic pipe subjected to the still air or to the central gas stream. As demonstrated later in detail, a perfect smooth liquid film develops along the inner acrylic wall, and a single ligament extends from the bottom end, evidencing that the current setup generates a liquid film with uniform thickness in the circumferential direction.

The central airflow is originally pressurized by the screw compressor and is reserved in the tank at the maximum pressure of 0.7 MPa. The total pressure is controlled using a precision regulator (IR3000, SMC). The airflow rate is monitored by a thermal mass flowmeter (Mass Flow Monitor, OVAL). Passing through the long stainless steel pipe, the air becomes a fully-developed turbulent flow. The airflow then enters the acrylic pipe to encounter the liquid film. The outlet of the acrylic pipe is open to the atmosphere.

We define the origin of the coordinate at the top of the test section, where the liquid film detaches from the stainless steel pipe. The x-axis indicates the axial direction, pointing vertically downward. The y-axis denotes the radial direction from the inner acrylic wall ($y = 0$) to the central axis.

The refractive indices of water, acrylic, and glycerol are $n_{water} = 1.33$, $n_{acrylic} = 1.49$, and $n_{glycerin} = 1.48$, respectively. The density of the water is $\rho_l = 1000$ kg/m^3, the coefficient viscosity is $\eta_l = 1.0$ mPa $\cdot$ s, the kinematic viscosity is $\nu_l = 1.0 \times 10^{-6}$ m^2/s, and the surface tension coefficient is $\sigma = 72.8$ mN/m. Based on the liquid film thickness of h, mean velocity of u_m, and the volume flow rate of Q, the liquid film Reynolds number is defined as $Re_l = Q/(\pi D_l \nu_l) = \rho_l u_m h/\eta_l$, which varies in $Re_l = 3 \sim 100$. The density of airflow is $\rho_g = 1.25$ kg/m^3, and the coefficient viscosity is $\eta_g = 1.8 \times 10^{-5}$ Pa $\cdot$ s. The airflow velocity is controlled in the range of $u_g = 7.0 \sim 30$ m/s, which corresponds to the gas Reynolds number $Re_g = \rho_g u_g D_l/\eta_g$ of $1.8 \times 10^4 \leq Re_g \leq 7.8 \times 10^4$.

Figure 1(b) shows the setup for PLIF imaging, wherein the camera and laser sheet are allocated surrounding the test section. We set the acrylic box (50×50×100 mm) filled with glycerol at the outside of the acrylic pipe to match the refection index between the acrylic pipe and the ambient. To capture axial cross-sectional images of the dyed liquid film, we set the high-speed camera (FASTCAM Mini AX100, Photron) and YAG double-wave sheet laser (RayPower2000, Dantec, wavelength of $\lambda = 532$ nm) at 90 degrees (see Fig. 1(c)). The imaging frame rate is 1000 Hz, and the number of pixels is $x \times y = 1024 \times 512$. Adopting a teleconverter (N-AF 2×TELEPLUS MC7×2, Kenko) to a long-distance microscopes (K2 DistaMax, INFINITY), we achieve high resolutions in space ($2.1 \sim 7.0$ μm/pixel). We attach a long-pass filter that transmits wavelengths of $\lambda > 550$ nm on the tip of the lens to selectively visualize fluorescence $\lambda \approx 570$ nm.

Inside the test section, the typical film thickness is $h \sim 10^{-4}$ m and corresponding viscous timescale is $\tau_\nu = h^2/\nu_l \sim 10^{-2}$ s. The film flow with $u_m \sim 10^{-1}$ m/s will reach the quasi-steady state at $x \gg \tau_\nu u_m \sim 10^{-3}$ m. Therefore, we select the measurement area of the liquid film at $x \geq 40$ mm.

3 Principle of T-PLIF

In this section, we explain the mathematical principle of T-PLIF along with step-by-step image analysis, with comparison to two typical PLIF-based methods based on the brightness threshold (threshold-based method) and the gradient of brightness (gradient-based method), as summarized in Table 1.

3.1 T-PLIF method

The feature of T-PLIF is to use *temporal variation* of a probability variable. As a simple and general problem depicted in Fig. 2(a), we consider a sinusoidal wave with its center of oscillation at $y = h$ and the half amplitude of unity, represented by $Y \equiv y - h = \sin(\omega t)$. Here, ω and t indicate angular velocity and time, respectively. The upper side of the wave $Y > \sin(\omega t)$ corresponds to the gas phase, and the lower side $Y \leq \sin(\omega t)$ denotes the liquid phase. Depending on the phase at each point, we define the probability variable of X as follows,

$$X = \begin{cases} 0 & \text{for gas phase} \\ 1 & \text{for liquid phase} \end{cases}. \tag{1}$$

Assuming that we stand at $Y = a$ $(-1 \leq a \leq 1)$, we alternatively experience both phases of gas and liquid in time. We deduce the probability of P that the position of $Y = a$ is in the liquid phase during a unit cycle,

Table 1: Measurement methods

Method	Detection of gas/liquid interface
T-PLIF (proposed in this work)	maximum temporal variance of brightness
Threshold-based	artificial brightness threshold in time-averaged image
Gradient-based	maximum gradient of brightness in time-averaged image

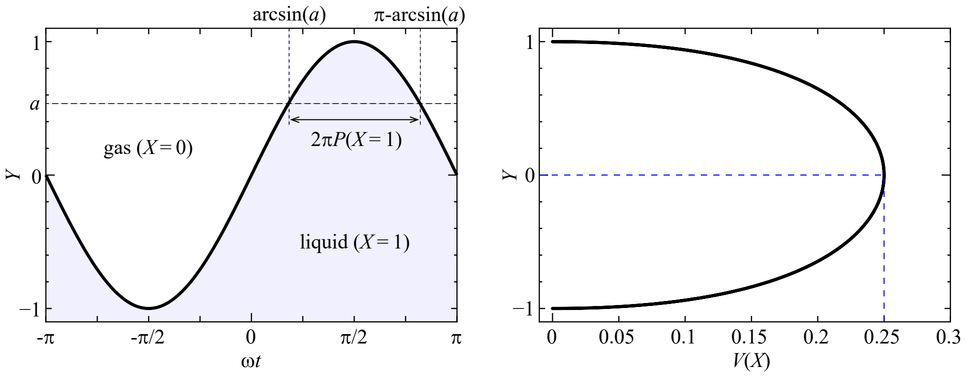

(a) Phase dependent probability variable of X (b) Temporal variance of X

Fig. 2: Schematic diagram of a sinusoidal wave

$$P(X = 1) = \frac{1}{2} - \frac{\arcsin a}{\pi}. \tag{2}$$

Then, we obtain the expected value $E(X)$, which is equivalent to $E(X^2)$,

$$E(X) = E(X^2) = \frac{1}{2} - \frac{\arcsin a}{\pi}. \tag{3}$$

We formulate the temporal variance $V(X)$ with respect to X by adopting the relationship of $V(X) = E(X^2) - E(X)^2$,

$$V(X) = \frac{1}{4} - \left(\frac{\arcsin a}{\pi}\right)^2. \tag{4}$$

As shown in Fig. 2(b), the variance reaches the maximum value of $V(X)_{\max} = 0.25$ at $a = 0$ or $y = h$, wherein the two phases appear with the probability of 50 % in each. The variance decreases away from the center of the oscillation. It is obvious that the variance is zero both at $Y > 1$ continuously in the gas phase and at $Y < -1$ in the liquid phase. Therefore, the variation of two-phase interface with sinusoidal oscillation is maximized at the time-averaged interfacial position. Inversely, the mean liquid thickness can be uniquely identified by detecting the maximum variance position of a phase-dependent scalar value with no use of any artificial threshold, which is the basic principle of the proposed T-PLIF method.

For the practical application of T-PLIF to measure the liquid film thickness, we employ the brightness value of 8-bit gray scale image for X, because the PLIF images show high-intensity and low-intensity (dark) areas which contain information of the liquid film and the gas-liquid interface with further calibration of the light path. Now we need to check whether it can be exploited for a corrugated, but not perfectly sinusoidal, liquid film, which is a general case in practical liquid film flow.

Figure 3 shows the sequential steps of T-PLIF from the acquisition of raw images to the measurement of the film thickness. As a case study, the experiments were conducted at $Re_l = 50$ with theoretical film thickness of $h = 0.24$ mm, image resolution of 3.8 μm/pixel and laser power of 1.2 W. To add fluctuations to the liquid film, we introduce slow airflow of $u_g = 7$ m/s ($Re_g = 1.8 \times 10^4$). (i) We record 5000 frames of cross-sectional images in 8-bit gray scale. Excited by the laser sheet, the dyed liquid film shows luminous on the left wall. However, the intensity of luminescence is weak as the film is thin. (ii) We obtain the brightness values $I(x, y)$ at every pixel of all frames, allowing for calculating the variance of $V(I(x, y))$ along with time. The figure depicts the result of $V(I)$ normalized to the 8-bit gradation image, wherein the bright area denotes a large variance. (iii) At each x coordinate, we detect the position of y corresponding to $V_{\max}$. We define the mean film thickness of h averaged in the x-direction. We also calculate the standard deviation (S.D.) and standard error (S.E.) of h. (iv) The figure shows the distribution of $V(I)$ at $x = 42$ mm, indicated by the yellow dashed line in (ii). By identifying the sharp peak of $V(I)_{\max}$, we can determine the value of h.

As demonstrated, the proposed T-PLIF method can clearly identify the mean film thickness with direct analysis of PLIF images with no need for artificial threshold of

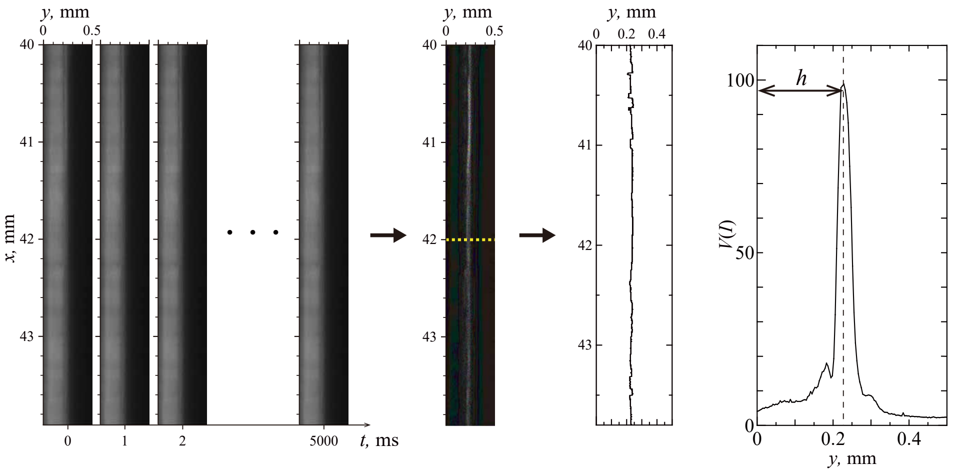

(i) Image acquisition to calculate $V(I(x, y))$ (ii) $V(I)$ (iii) Detect posotion at $V(I)_{\max}$ (iv) $V(I)$ at $x = 42$ mm

Fig. 3: Image analysis process of T-PLIF. This identifies the location of maximum variation and detects the interface.

brightness, smoothing function, or calibration data between I and h. We also note that the images need not to be binarized throughout the analysis.

Besides, T-PLIF also provides an appropriate threshold for detecting the time-averaged position of the gas-liquid interface. In Section 4.4, the T-PLIF method is combined with the threshold-based PLIF method for analyzing unsteady liquid films.

3.2 Threshold-based and gradient-based methods

Figure 4(a) shows the analysis process of the threshold-based method. (a.i) We obtain the time-averaged image consisting of $\langle I(x, y)\rangle$ based on the captured images. (a.ii) Then, we binarize the time-averaged image using an arbitrary threshold value (here, $\langle I\rangle = 60$), indicating the mean film thickness position. (a.iii) At each x position, we detect the pixel of y, whose brightness is equivalent to the threshold. (a.iv) The figure shows the profile of $\langle I(x, y)\rangle$ at $x = 42$ mm before binarized. $\langle I(x, y)\rangle$ reaches the peak value around $y = 0.08$ mm, then decreases as away from the wall. The mean thickness of corrugated liquid film doesn't coincide with the position of the maximum luminous intensity, indicating the dependence of the measurement result on the non-physical threshold value.

Figure 4(b) depicts the procedure of the gradient-based method. (b.ii) In this method, we calculate $-\partial\langle I\rangle/\partial y$ for all the pixels (distribution of normalized result of $-\partial\langle I\rangle/\partial y$). (b.iii) We identify the y-position at the maximum value of $-(\partial\langle I\rangle/\partial y)$ as the mean interface height. (b.iv) The figure shows the profile of $-\partial\langle I\rangle/\partial y$, in which a distinguishable peak value appears. When the original brightness is small due to small film thickness, the 1st and 2nd peaks of $-\partial\langle I\rangle/\partial y$ can be close, indicating another source of error.

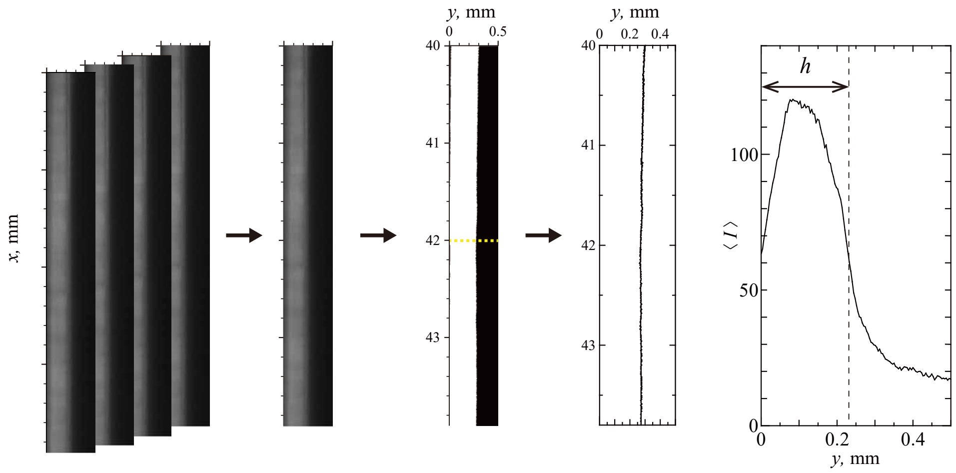

(i) Image acquisition to calculate ⟨$I(x, y)$⟩ (ii) Binarized ⟨ I ⟩ (iii) Detect posotion at ⟨ I ⟩ = 20 (iv) ⟨ I ⟩ at x = 42 mm

(a) Threshold-based method

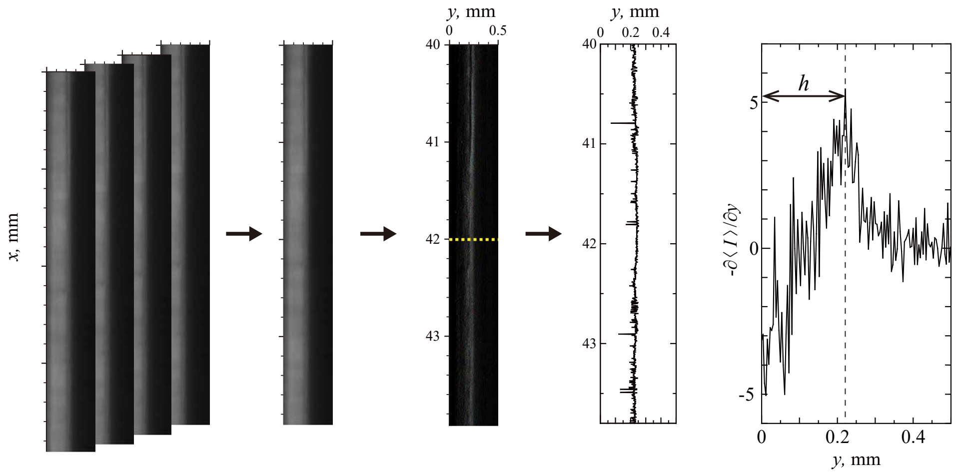

(i) Image acquisition to calculate ⟨$I(x, y)$⟩ (ii) $-\partial\langle I\rangle/\partial y$ (iii) Detect posotion at $-\partial\langle I\rangle/\partial y$ max (iv) $-\partial\langle I\rangle/\partial y$ at x = 42 mm

(b) Gradient-based method

Fig. 4: Image analysis processes

4 Results and discussion

We first present visualization results of the liquid film flow and derive theoretical formulations of the thickness as reference data. Then, we examine the ray-tracing analysis for the present annular flow, followed by the measurement results of the liquid film thickness to examine the proposed T-PLIF method at low and high air velocity. Finally, we extend T-PLIF to unsteady measurement of wavy films.

4.1 Overview of the film flow

Figure 5(a) shows the backlight images of laminar liquid film at different Re_l conditions without airflow ($u_g = 0$ m/s). At $Re_l = 3$, the smooth liquid film flows on the inner acrylic pipe with no waviness. At the bottom end, the liquid film gathers at the central axis due to surface tension, forming the single ligament, which evidences the liquid film flow at a steady state with homogeneous thickness in the circumferential direction. The

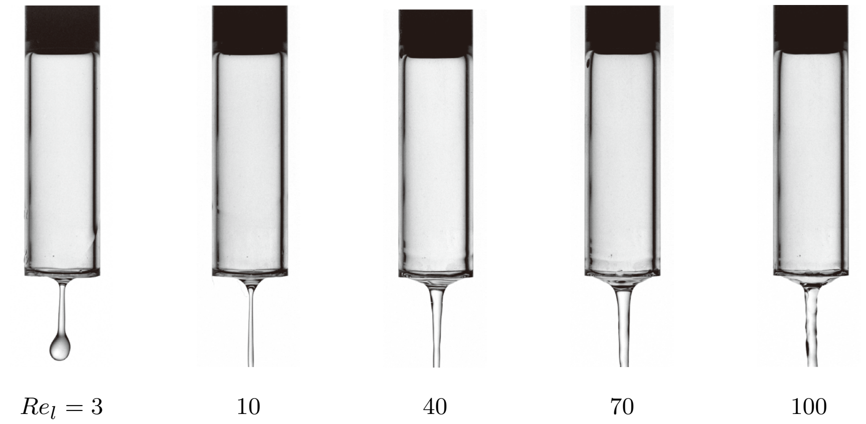

(a) Without central airflow ($u_g = 0$ m/s)

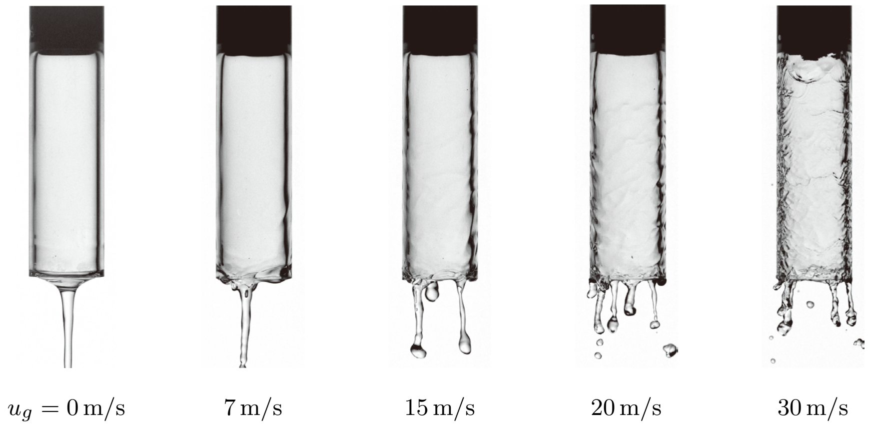

(b) With airflow at $Re_l = 50$

Fig. 5: Visualization results of liquid film flow

elongating ligament is periodically pinched to produce a droplet through the Plateau-Rayleigh instability. As Re_l increases, the liquid film keeps smooth, while the length of the ligament becomes longer before disintegrates.

Figure 5(b) shows the liquid film at $Re_l = 50$ subjected to airflow with different u_g. At $u_g = 7$ m/s, long waves with small amplitude form from the Kelvin-Helmholtz (KH) instability. The gas pressure breaks the accumulated liquid film at the bottom end, producing single ligaments connected to the trailing edge, no longer on the central axis. With increasing $u_g \geq 20$ m/s, the film becomes more unstable with shortened axial wavelength and three-dimensional fluctuations, followed by the several ligaments extending downwards driven by the Rayleigh-Taylor instability. We notice that the number of ligaments increases with increasing gas velocity.

By introducing an interfacial friction factor f, we express the shear stress of the gas flow acting on the liquid film.

$$\tau = \frac{1}{2} f \rho_g u_g^2 \tag{5}$$

From the one-dimensional Navier-Stokes equation, we derive the velocity profile of the steady film flow subjected to the shear stress and gravity with considering the film viscous stress.

$$u_l(y) = -\frac{gy^2}{2\nu_l} + \frac{gyh}{\nu_l} + \frac{\tau y}{\eta_l} \tag{6}$$

The film thickness h is derived as a function of Re_l (Alekseenko and Nakoryakov 1995).

$$\frac{gh^3}{3\nu_l} + \frac{\tau h^2}{2\mu_l} = Re_l \nu_l \tag{7}$$

When the shear stress of the gas flow is negligible compared to gravity ($\tau \ll \rho_l g h$), h is given simplify as follows (Nusselt 1916);

$$h = \left(\frac{3\nu_l^2 Re_l}{g} \right)^{1/3}. \tag{8}$$

When u_g increases to become $\tau \gg \rho_l g h$ and the thin liquid film follows the Couette flow pattern, h is expressed as (Inoue and Maeda 2021, Inoue et al. 2022);

$$\frac{h}{D_l} = \frac{2}{\sqrt{f}} \frac{\eta_l}{\eta_g} \sqrt{\frac{\rho_g}{\rho_l}} Re_l^{1/2} Re_g^{-1}. \tag{9}$$

Due to the large velocity gap between the mean liquid velocity u_m and u_g, the KH instability induces axial waviness with a wavelength of λ. Assuming the wave amplitude being much smaller than λ, f can be evaluated by the Blasius correlation $f = 0.08 Re_g^{-1/4}$ (Nikuradse 1933, Moody 1944, Schlichting and Gersten 2016). The vorticity thickness of $\delta = 2D/(f Re_g)$ determines λ independent of the capillary force (Rayleigh 1895, Villermaux 1998),

$$\lambda \approx \delta \sqrt{\frac{\rho_l}{\rho_g}}. \tag{10}$$

The wave propagates faster than u_m with the phase velocity (Dimotakis 1986),

$$u_c = \frac{u_m \sqrt{\rho_l} + u_g \sqrt{\rho_g}}{\sqrt{\rho_l} + \sqrt{\rho_g}}. \tag{11}$$

Irrespective of u_g, we emphasize that the liquid is uniformly supplied and the time-averaged thickness of wavy film becomes circumferentially homogeneous inside the pipe, allowing for the measurement of film thickness at any cross section for the validation of T-PLIF.

4.2 Ray Tracing

Before measuring the film thickness, we conduct optical path analysis with the present PLIF setup. This is necessary to manifest the relationship between the actual film thickness and the obtained PLIF image. We denote the ray tracing method in detail in Appendix A and the experimental validation in Appendix B. Figure 6(a) shows a schematic of ray tracing analysis assuming an ideal smooth surface. The laser sheet has a thickness of $h_L \approx 0.5$ mm, which illuminates the plane parallel to the camera sensor with a deviation of ΔX away from the central line of the acrylic pipe. We confirmed the negligible effect of refraction at the glycerin/acrylic and acrylic/water interfaces on the illuminating plane. In addition, as ΔX is much smaller than D_l, the film thickness illuminated by the laser sheet can be regarded as equivalent with h.

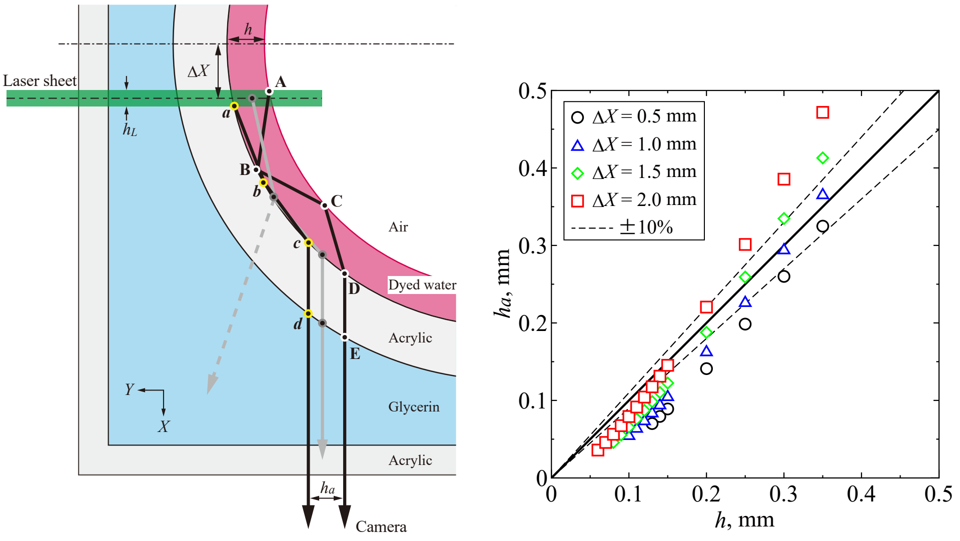

(a) Schematic of ray tracing (top view) (b) True film thickness against PLIF image

Fig. 6: Ray tracing analysis

Here, we consider the ray traveling perpendicular to the camera sensor for $\Delta X = 1.5$ mm and $h = 0.2$ mm. From Point A, the ray is emitted, which depicts the liquid/gas interface, reaching Point B on the inner wall of acrylic pipe. The incident angle on Point B is 78 degrees, and the reflection rate is 0.16 based on the Fresnel equation (Born and Wolf 2013). The reflected ray on Point B is totally reflected at Point C on the interface. Then, it proceeds refracted at Points D and E, finally traveling parallel to the camera axis. Emitted from the solid/liquid interface on Point a, the ray of luminescence is reflected at Point b, where the incident angle is 85 degrees and the reflection rate is 0.46. The ray is then refracted at Points c and d, reaching the camera.

The ray emitted from the middle of the laser, indicated by the gray line, also follows the same path $abcd$ near the wall. It eventually switches to path ABCDE at $y \approx 0.08$ mm. For the light emitted from $y = 0.08$ mm, the angle of incidence to Point b is 82 degrees and to Point B is 83 degrees, which is very close, resulting in unclear boundary in the brightness distribution of the visualized image (see Fig. 7(b)). The ray refracted at the water-acrylic interface, shown by the dashed line, does not reach the camera. In an obtained PLIF image, the film thickness corresponds to the distance between the two parallel rays of h_a at the exit, which depends on ΔX.

Figure 6(b) shows the analysis result of the relationship between h and h_a at $\Delta X = 0.5 \sim 2.0$ mm, where h_a reasonably agrees with h. As ΔX increases at constant h, the ray from Point A, traveling a longer path than the ray from Point a, arrives at the camera shifting in the $-Y$-direction. Then, the film thickness tends to be thicker, which was experimentally confirmed as well. We notice that the gradient of the slope is steeper than unity at a fixed ΔX. Based on the result of the ray tracing, we finally fix the optical arrangement as $\Delta X = 2.0$ mm for $Re_l \leq 20$ (i.e., $h < 0.2$ mm) and as $\Delta X = 1.5$ mm for $Re_l > 20$.

4.3 Measurement of the mean film thickness

We impose a slow airflow of $u_g = 7$ m/s for adding perturbation to the film flow. As discussed in the next section, T-PLIF is not applicable to a perfectly smooth liquid film (with no waviness). To validate the proposing T-PLIF, we vary the film flow conditions in a range of $Re_l = 3 \sim 100$ to compare the results of mean thickness with Eq. (7). Three cases of resolution in space are exploited to resolve the cross sectional image, i.e., fine, middle, and coarse, with resolutions of 2.1, 3.8, and 7.1 μm/pixel, respectively.

We first confirm the dependency of film thickness on the laser power at a fixed film flow condition of $Re_l = 50$. Figure 7(a) shows the measurement results of h resolved by 3.8 μm/pixel against the laser power up to 2 W compared with the theoretical result of $h = 0.24$ mm. The error bars indicate standard derivation (S.D.) of the mean film thickness. The results of T-PLIF agree well with the theoretical results with $\varepsilon = 5$ % discrepancy in average regardless of the laser power (maximum deviation of $\varepsilon_{\max} = 8$ %). Except for the case of 0.6 W, the S.D. is small. For threshold-based method, the threshold is set as $\langle I \rangle = 60$. The measurement results increase as the laser power becomes strong, indicating that the calibration is necessary depending on the laser power. The results of the gradient-based method provide the constant thickness against laser power, while the S.D. is larger than the results of T-PLIF.

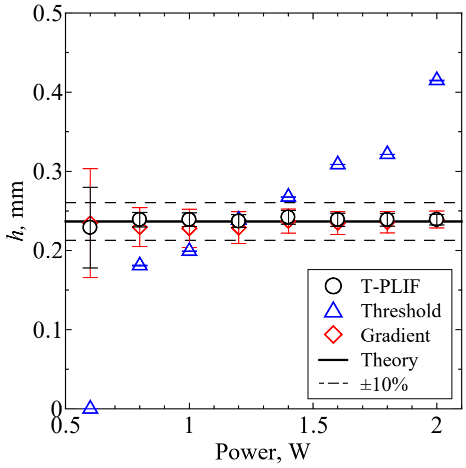

(a) Mean film thickness

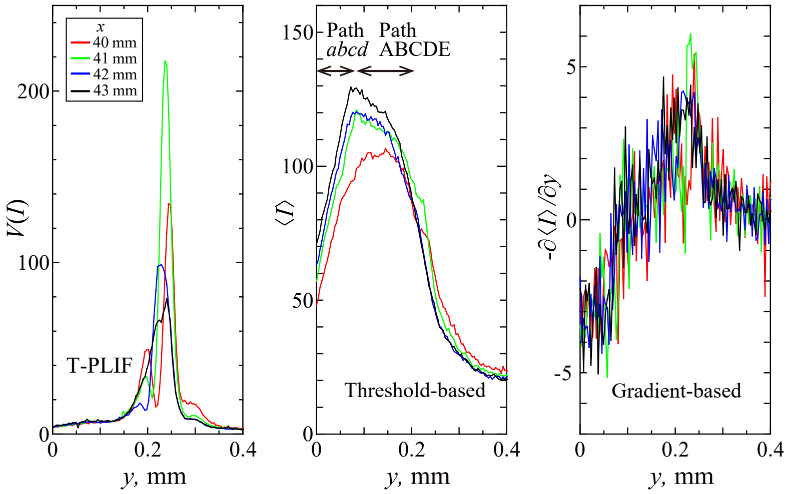

(b) Distribution of index at laser power of 1.2 W

Fig. 7: Effect of laser power on film thickness. (a)Error bars indicate S.D.

Figure 7(b) shows the distributions of the indices of each method calculated at $x = 40 \sim 43$ mm with the laser power of 1.2 W. In the case of T-PLIF, we can clearly identify the position in the y-direction corresponding to $V(I)_{\max}$ for all the x positions. The distribution of $V(I)$ is smooth with remarkable peak value, consistent with the small S.D. plotted in Fig. 7(a). Therefore, T-PLIF can measure the local mean film thickness along the x-direction. For threshold-based method, the profiles of $\langle I \rangle$ depict a similar trend. The y positions corresponding to $\langle I \rangle = 60$ are identical.

The maximum value of $\langle I \rangle$ appears inside the film, because the strong luminescence emitted from the central laser sheet between Point A and Point a in Fig. 6(a) proceeds in the middle of the rays to reach the camera. For the gradient-based method, the gradient value of $-\partial\langle I \rangle/\partial y$ largely fluctuates due to the small noise superposed to $\langle I \rangle$. The fluctuation leads to mis-detection of the film thickness, resulting in the large S.D. with the gradient-based method. Adopting a smoothing fitting to $\langle I \rangle$ may help to reduce the noises in the distribution curve of $-\partial\langle I \rangle/\partial y$.

In the following, we set the laser power as 1.2 W. Figure 8(a) shows the experimental results of the mean film thickness at $Re_l = 3 \sim 100$ with a fine image resolution, in comparison to the theoretical results by Eq. (7). The results of T-PLIF demonstrate good agreement for the film thickness of $h > 0.2$ mm with the theoretical results at the discrepancy of $\varepsilon \leq 9$ %. However, in the thin film condition of $h \leq 0.2$ mm, the results of T-PLIF overestimate the theoretical reference at $\varepsilon = 20$ %. As shown in Fig. 7(b), the fluorescence also appears in the gas phase across the blurred interface, which causes the overestimation by T-PLIF typically at the thin liquid film. The distributions of $V(I)$ for $Re_l = 10$ and $Re_l = 100$ in Fig. 8(b) show that the widths of the distributions are different. For $Re_l = 10$, fluctuations of brightness appear over a wide range near the interface. At $y = 0$ mm (liquid phase) and $y = 0.4$ mm (gas phase), the value of $V(I)$ is small, but non-zero, as a result of the reflection and transmission of luminescence on the liquid/gas and liquid/solid interfaces due to the background noises. For the threshold-based method, the threshold value is set as $\langle I \rangle = 60$. The results correctly indicate the trend of the theoretical curve over a wide range, including $h < 0.2$ mm, while the measurement values at $h > 0.2$ mm show deviations of $\varepsilon_{\max} = 15$ %. This is because the luminescence that is emitted from the thick film

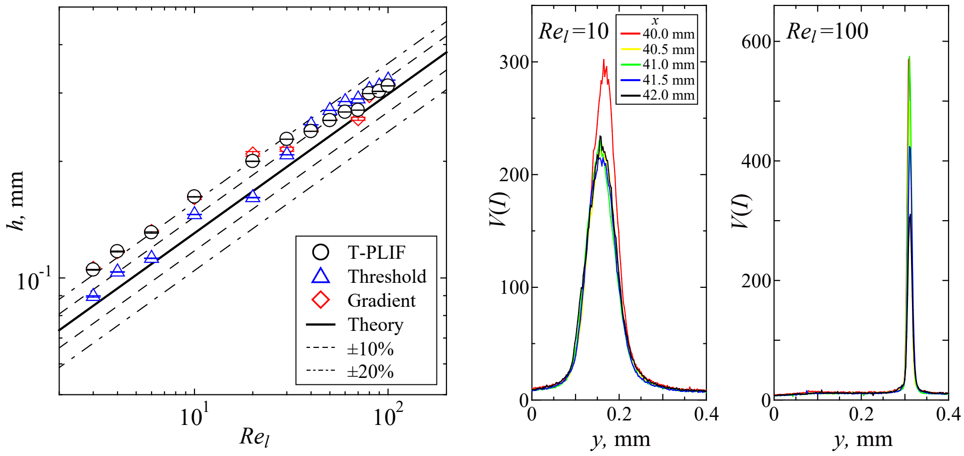

(a) Mean film thickness

(b) Distribution of $V(I)$ in T-PLIF

Fig. 8: Measurement results of film thickness at fine space resolution (2.1μm/pixel). (a)Error bars indicate S.E.

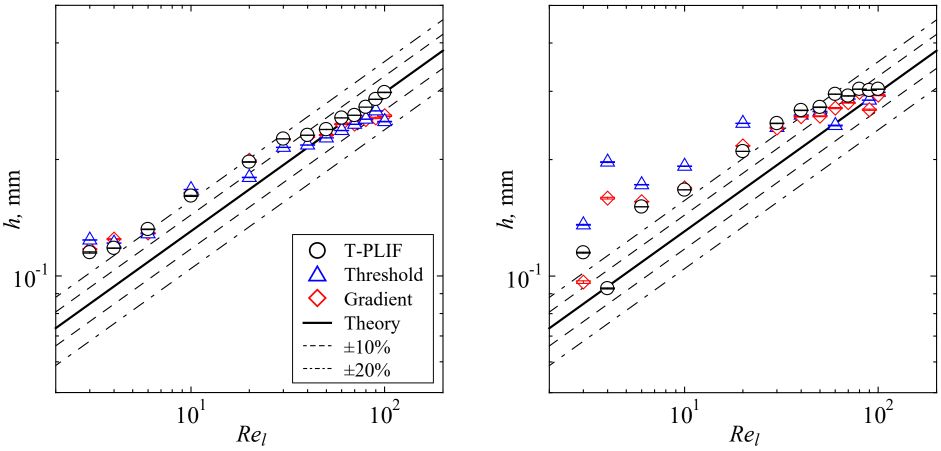

(a) Middle resolution (3.8μm/pixel) (b) Coarse resolution (7.1μm/pixel)

Fig. 9: Effect of space resolution

naturally becomes bright, and the constant threshold value detects the outside edge of the oscillating film (see Appendix C). The results of the gradient-based method reproduce the theoretical results, similar to those of T-PLIF. The small S.E. is attributed to the large number of sampling cases of 1024 pixels in the x-direction.

Figures 9(a)(b) show the results at middle and coarse resolutions in space, respectively. In Fig. 9(a), the results of T-PLIF agree with the theoretical values within an accuracy of $\varepsilon = 2$ % ($\varepsilon_{\max} = 6$ %) for $h > 0.2$ mm. However, for $h < 0.2$ mm, the experimental results deviate from the theoretical curve for all methods. In Fig. 9(b), T-PLIF shows a good agreement with a deviation of $\varepsilon < 10\%$ for $h > 0.28$ mm. For $h < 0.28$ mm, i.e., when the liquid film is captured with fewer than 40 pixels, the experimental results deviate significantly from the theoretical values for all methods.

4.4 Effect of airflow velocity

With varying airflow velocity of $u_g = 0 \sim 30$ m/s, we measure the liquid film thickness at $Re_l = 50$ with a fine image resolution. Figure 10(a) shows the experimental results obtained with the three methods and the theoretical values calculated with Eqs. (7)-(9). At $u_g = 0$ m/s, the film thickness derived from Eq. (7) matches that of Eq. (8). However, as u_g increases, the film thickness asymptotically follows Eq. (9), thinning as $h \propto u_g^{-7/8}$.

We first discuss the case without airflow $u_g = 0$ m/s. In this condition, the liquid film is smooth with no waviness as confirmed in Fig. 5(a). Since T-PLIF essentially requires a time variance of the luminescent brightness to calculate $V(I)$, it is unable to detect the correct thickness of the smooth film. In such cases, the threshold-based method with threshold of $\langle I \rangle = 60$ and the gradient-based method correctly measure the thickness close to the theoretical result.

By increasing the gas velocity to $u_g \geq 7$ m/s, T-PLIF reproduces the theoretical trend, while T-PLIF overestimates the theoretical value by up to 25 %. The overestimation of liquid films thinner than 0.2 mm is consistent with the results in Fig. 8(a). Figure 10(b) indicates the clear peaks of $V(I)_{\max}$ at $u_g = 25$ m/s, validating the feasibility of T-PLIF in processing wavy films driven by the shear force of airflow. The threshold-based method overpredicts the film thickness due to the inappropriate threshold value. With a fixed threshold value, the results of the threshold-based

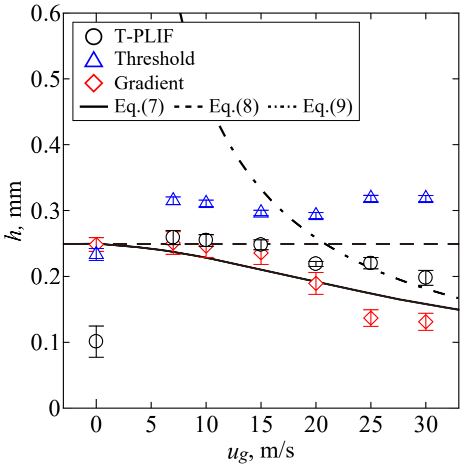

(a) Mean film thickness. Error bars are S.E.

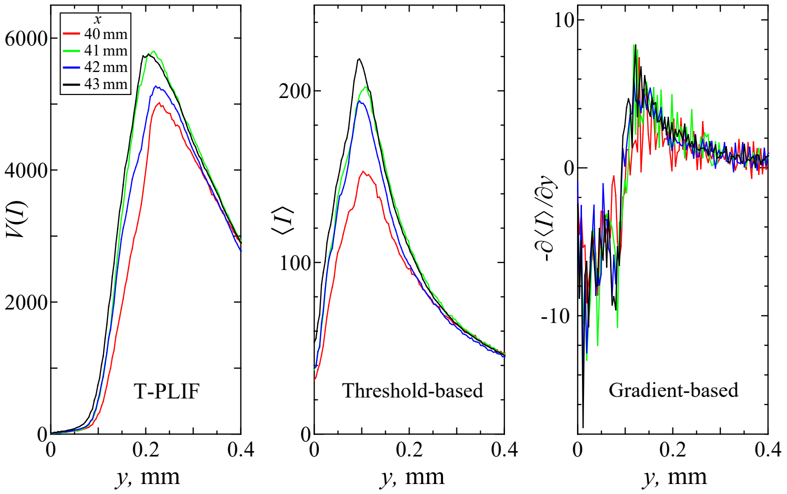

(b) Distribution of index at $u_g = 25$ m/s

Fig. 10: Effect of u_g on film thickness.

method are consistently thicker than the theoretical results. By adjusting the threshold value to $\langle I\rangle = 100$, we may obtain correct experimental results close to the theoretical curve. This fact indicates that the threshold-based method is applicable mainly for measuring known film thickness, where the threshold value can be properly predetermined. The gradient-based method can measure the thickness, while the S.E. is larger in comparison to the results of T-PLIF. It also underestimated the film thickness rather than the theoretical curve. The position of $\langle I\rangle_{\max}$ is located inside the liquid film at $y \approx 0.1$ mm, and the value of $\langle I\rangle$ gradually decays at $y > 0.1$ mm. As the wave amplitude increases, the position of $-(\partial\langle I\rangle/\partial y)_{\max}$ no longer corresponds to the mean liquid/gas interface and exists inside the film, resulting in misdetection of the interface.

We further combine T-PLIF and the threshold-based method to characterize the unsteady liquid film dynamics. Comparing the results of T-PLIF and the threshold-based method in Fig. 10(b), the threshold value of $\langle I\rangle$ is set as 100 for the threshold-based method. Figure 11 indicates the liquid-gas interface in the $x - y$ plane propagating over time, t. The height of the liquid film is colored by the contour. The wave crest at $(x, t) = (40\text{ mm}, 10\text{ ms})$ propagates downstream reaching $(x, t) = (44\text{ mm}, 20\text{ ms})$ as depicted by the time series of backlit images. With the following wave crests and bottoms periodically, the mean film thickness is $h \approx 0.25$ mm, and the maximum height is $h_{\max} \approx 0.5$ mm, indicating that the amplitude is equivalent with the mean thickness, consistent with the experimental study by Shinan et al.

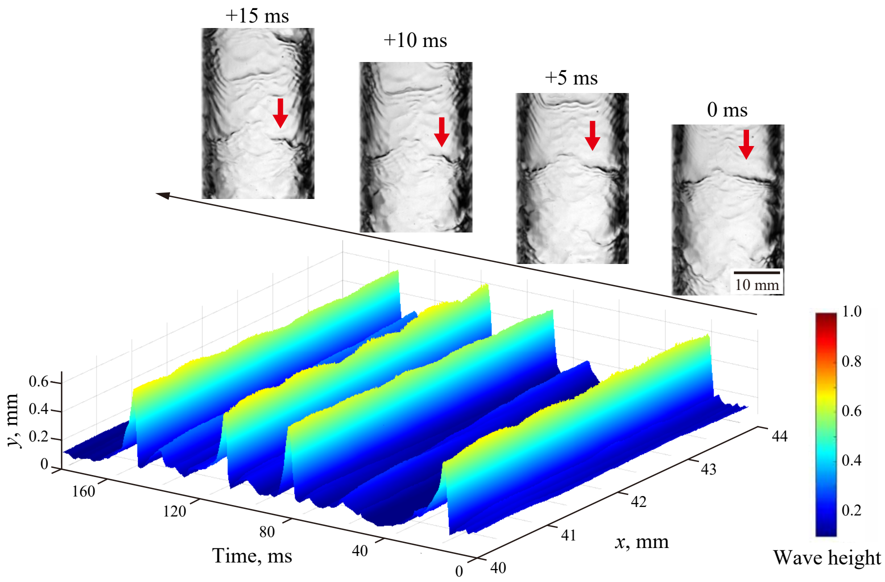

Fig. 11: Detected 2-dimensional wave structure along time at $u_g = 25$ m/s. Backlit images (top) and analyzed results (bottom) are separately conducted. Top: Red arrows track the same wave.

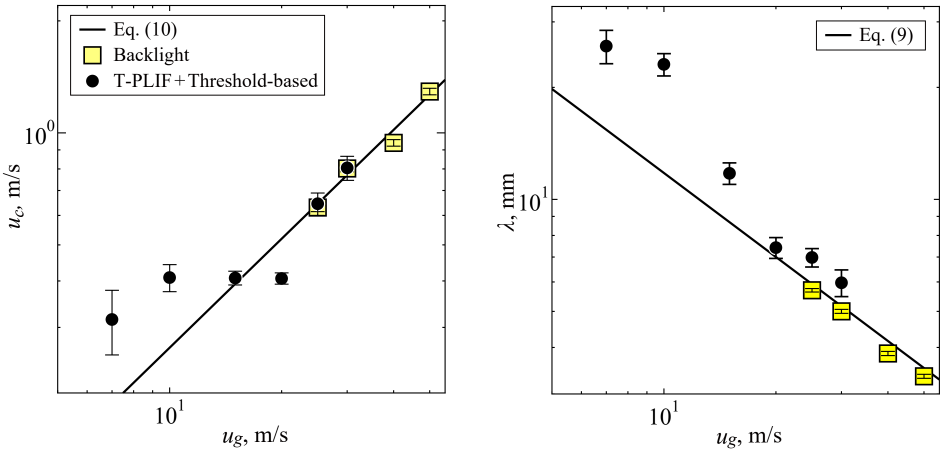

(a) Phase velocity (b) Axial wavelength

Fig. 12: Unsteady wave characteristics. Error bars indicate S.E.

(2019). However, the combined threshold-based method is time-dependent, and should be further evaluated in measuring instantaneous film thickness.

At last, we quantitatively measure the phase velocity u_c of each wave and axial wavelength λ based on the combined method of T-PLIF and threshold-based method. Figure 12(a) shows the experimental results of u_c against u_g with the theoretical result of Eq. (11). At $u_g \geq 25$ m/s, we directly measure u_c from the backlit images by tracking waves in Lagrangian form, showing good agreement with the theoretical curve. We find that the results of the combined method (T-PLIF + threshold-based method) at $u_g = 25,\ 30$ m/s coincide well with the theoretical and backlit measurement results, wherein the wave is stimulated by the airflow. At the condition of $u_g < 20$ m/s, the gas shear is weak and Eq. (11) is no longer applicable, showing deviations with experimental results of the combined method. In Fig. 12(b), the results of λ based on the present combined method at $u_g = 25,\ 30$ m/s agree well with the theoretical result of Eq. (10) and backlit measurement results. As the shear force of airflow decreases at $u_g < 20$ m/s, the instability is suppressed with a longer wavelength.

As demonstrated, by identifying the adequate threshold brightness with T-PLIF, we successfully detect the liquid/gas interface and quantify the characteristics of wavy liquid film sheared by concurrent airflow. T-PLIF can provide the threshold value at each pixel along the x-direction for the threshold-based method, which compensates the non-uniform power and thickness of the laser sheet, thus efficiently improving the reliability and accuracy of unsteady measurement of wavy liquid films.

5 Conclusion

In this research, we propose and validate a new method of T-PLIF (time-variant PLIF) to alleviate difficulties in existing LIF-based techniques that require artificial threshold values of brightness/brightness gradient, post image processing, and calibration data between the brightness and the film thickness. We applied T-PLIF to a well-controlled annular liquid film flow, whose thickness follows the theoretical curves considering the effects of gas shear and gravity. We collect time-resolved PLIF images of water film with fluorescent dye using a high-speed camera and laser sheet, and use them to test the feasibility of the proposed method. By employing the time-variant brightness as the phase-distinguishing function, we successfully identify the time-averaged liquid-gas interface which exactly corresponds to the position with the maximum time-variance as mathematically proven. The distribution of time-variant brightness shows a unique and sharp peak, minimizing the standard error of the mean thickness. We demonstrated the feasibility of T-PLIF in cases of the mean film thickness of $h > 0.2$ mm with the error of $\varepsilon \leq 10\%$ compared to the theoretical value using an optical setup of 3.8μm/pixel or less. For thinner films, T-PLIF overestimated approximately $\varepsilon = 20\%$ including the accompanying shearing gas up to 30 m/s. In the whole process from raw image acquisition to the measurement of film thickness, T-PLIF does not need pre-defined threshold values or pre-acquired calibration data. Finally, by determining the threshold brightness by T-PLIF, the instantaneous liquid-gas interface was detected, which well characterizes the dynamics of wavy liquid film including the phase velocity and wavelength.

Appendix A: Ray tracing in detail

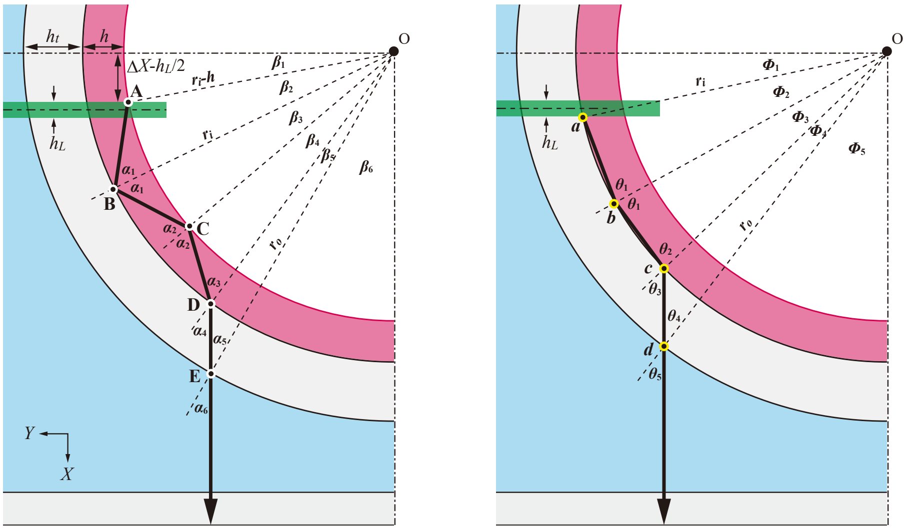

(a) From liquid/gas interface

(b) From solid/liquid interface

Fig. 13: Ray tracing model from luminescent liquid film

We describe the formulations adopted for the ray-tracing analysis. As shown in Fig. 13, we denote the inner diameter of the acrylic pipe as r_i, the outer diameter as r_o, the incidence and refraction angles as α and θ, and the angles between the pipe center and each point as β and ϕ. For the ray emitted from Point A on the liquid/gas interface in Fig. 13(a), the symmetry of the reflection and external angles yields the following relationships between α and β,

$$\begin{cases} \beta_1 &= \arcsin(\frac{X-h_L/2}{r_i-h}) \\ \beta_2 &= \beta_3 = \beta_4 = \alpha_2 - \alpha_3 \\ \beta_5 &= \alpha_4 - \alpha_5 \\ \beta_6 &= \alpha_6 \end{cases}. \tag{12}$$

Here, Snell's law and the sine theorem deduce the incidence and refraction angles of α. Considering that the summation from β_1 to β_6 is 90 degrees and the exit ray should be parallel to the camera axis, we derive equation for the exit angel of α_6,

$$\begin{aligned} &\arcsin\left(\frac{X-h_L/2}{r_i-h}\right) \\ &\quad + 3\left\{\arcsin\left(\frac{n_{glycerin}}{n_{water}}\frac{r_o}{r_i-h}\sin\alpha_6\right) - \arcsin\left(\frac{n_{glycerin}}{n_{water}}\frac{r_o}{r_i}\sin\alpha_6\right)\right\} \\ &\quad + \left\{\arcsin\left(\frac{n_{glycerin}}{n_{acrylic}}\frac{r_o}{r_i}\sin\alpha_6\right) - \arcsin\left(\frac{n_{glycerin}}{n_{acrylic}}\sin\alpha_6\right)\right\} + \alpha_6 = \frac{\pi}{2}. \end{aligned} \tag{13}$$

Similarly, for the ray from Point a on the solid/liquid interface in Fig. 13(b), θ and ϕ are connected through the following relationships,

$$\begin{cases} \phi_1 &= \arcsin(\frac{X+h_L/2}{r_i-h}) \\ \phi_2 &= \phi_3 = \pi - 2\theta_1 \\ \phi_4 &= \theta_3 - \theta_4 \\ \phi_5 &= \theta_5 \end{cases}. \tag{14}$$

The sum of ϕ_1 to ϕ_5 is obviously 90 degrees. θ_5 is constrained by the following equation,

$$\begin{aligned} &\arcsin\left(\frac{X+h_L/2}{r_i-h}\right) + 2\left\{\pi - 2\arcsin\left(\frac{n_{glycerin}}{n_{water}}\frac{r_o}{r_i}\sin\theta_5\right)\right\} \\ &\quad + \left\{\arcsin\left(\frac{n_{glycerin}}{n_{acrylic}}\frac{r_o}{r_i}\sin\theta_5\right) - \arcsin\left(\frac{n_{glycerin}}{n_{acrylic}}\sin\theta_5\right)\right\} + \theta_5 = \frac{\pi}{2}. \end{aligned} \tag{15}$$

Finally, we solve Eqs. (13)(15) numerically to derive h_a,

$$h_a = r_o(\sin\phi_5 - \sin\beta_6). \tag{16}$$

Appendix B: Experimental validation of ray tracing

We experimentally validate the present ray tracing method with the setup in Fig. 14(a). Inside the acrylic box (same as the one in Figs. 1(b)(c)) partially filled with glycerin, we allocate the acrylic pipe at the center partially filled with water. The water surface positions are higher than the glycerin surface. When we project the laser sheet from the front of the page with the displacement of ΔX from the center, there are three paths of ray, depicted by Path (i)∼(iii); Path (i) travels starting from the acrylic box wall, air, pipe walls (front and back), and acrylic box wall; Path (ii) sequentially traces the acrylic box, air, pipe wall, water, pipe wall, air, and acrylic box; Path (iii) goes through the acrylic box, glycerin, pipe wall, water, pipe wall, glycerin, and acrylic box. We set a projection screen at $L = 1$ m away from the pipe center to measure the three arrival positions of the laser sheet passing through each ray path with different displacements of $\Delta X = 1.25, 2.25, 4.25,$ and 6.25 mm. Since the water fills the pipe to the height, a distinction from the experiment in Fig. 6 is that reflection on the water interface is not analyzed, while the analysis procedure including the refraction in the media is consistent.

Figure 14(b) illustrates the rays depending on the refractive indices of the medium. We express the incident and refraction angles of α as a function of ΔX.

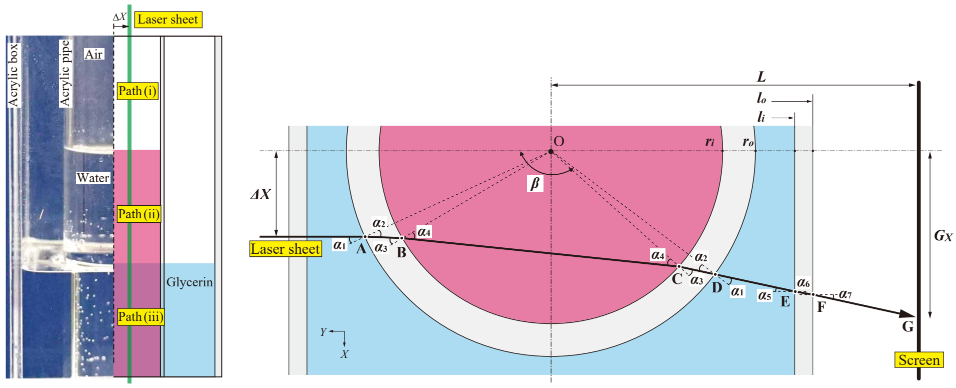

(a) Schematic setup (b) Model of refracting ray of light

Fig. 14: Experiment and analysis of tracing rays through three different paths

$$
\begin{cases}
\alpha_1 & = \arcsin(\frac{\Delta X}{r_o}) \\
\alpha_2 & = \arcsin(\frac{n_{glycerin}}{n_{acrylic}} \frac{\Delta X}{r_o}) \\
\alpha_3 & = \arcsin(\frac{n_{glycerin}}{n_{acrylic}} \frac{\Delta X}{r_i}) \\
\alpha_4 & = \arcsin(\frac{n_{glycerin}}{n_{water}} \frac{\Delta X}{r_i}) \\
\alpha_5 & = -2\alpha_1 + 2\alpha_2 - 2\alpha_3 + 2\alpha_4 \\
\alpha_6 & = \arcsin(\frac{n_{glycerin}}{n_{acrylic}} \sin\alpha_5) \\
\alpha_7 & = \arcsin(\frac{n_{glycerin}}{n_{air}} \sin\alpha_5)
\end{cases}
\tag{17}
$$

Here, the values of $n_{glycerin}$ and n_{water} are replaced by $n_{air} = 1$, when a ray passes through air instead of glycerin and water. We also deduce the angle of β with the center at Point D.

$$
\beta = \pi + \alpha_1 - 2\alpha_2 + 2\alpha_3 - 2\alpha_4 \tag{18}
$$

We finally formulate the arrival position G_X in the X-direction on the screen.

$$
G_X = r_o \sin\beta + (l_i - |r_o \cos\beta|) \tan\alpha_5 + (l_o - l_i) \tan\alpha_6 + (L - l_o) \tan\alpha_7 \tag{19}
$$

Figure 15 presents the measured and calculated results of G_X on the screen. We confirm the good agreement for the three divided ray paths, convincing the validity of the basics of the ray tracing analysis and the derived formulations. The validation also evidences the reliability of the values of refractive indices.

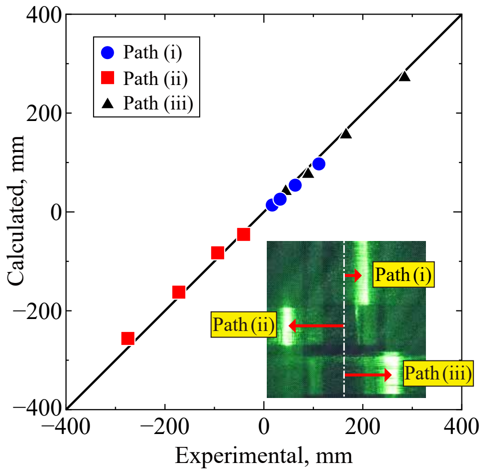

Fig. 15: Relationship between experimental and calculated results of laser sheet displacement on the screen. The snapshot shows the three rays divided on the screen.

Appendix C: Effect of threshold value of brightness

The threshold-based method identifies the liquid-gas interface based on the artificial threshold of brightness. Figure 16 shows the results of the film thickness for different threshold values with a fine image resolution. It shows that small value of threshold tends to overpredict the film thickness. By setting the value to 60 (valid limited to this case), the results follow the theoretical reference line, indicating that an appropriate threshold is necessary for the threshold-based method - this can be determined by T-PLIF as demonstrated in Sec. 4.4.

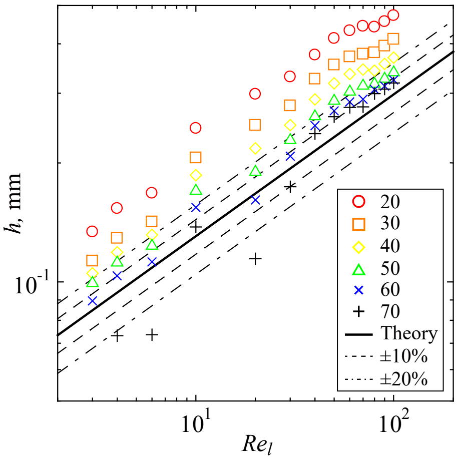

Fig. 16: Effect of threshold on mean film thickness in threshold-based method at $Re_l = 50$ without airflow.

Acknowledgments

This work was supported by JST SPRING, Grant Number JPMJSP2136.

Declarations

Ethical Approval

Not applicable, because this article does not contain any studies with human or animal subjects.

Funding

Y.K. was supported by JST SPRING, Grant Number JPMJSP2136.

Availability of data and materials

The data that support the findings of this study are available from the corresponding author upon reasonable request.

References

Weinstein, S.J., Ruschak, K.J.: Coating flows. Annu. Rev. Fluid Mech. **36**, 29–53 (2004) https://doi.org/10.1146/annurev.fluid.36.050802.122049

Fujii, G., Daimon, Y., Furukawa, K., Inoue, C., Shiraiwa, D., Tanaka, N.: Visualization of coolant liquid film dynamics in hypergolic bipropellant thruster. J. Propuls. Power **38**(2), 267–273 (2022) https://doi.org/10.2514/1.B38421

Wu, S.-Y., Zhou, S.-Y., Xiao, L., Chen, L., Chen, Z.-L.: Experiment on liquid film flow and heat transfer of laminar liquid jet impacting on cylindrical surface. Phys. Fluids **35**(2) (2023) https://doi.org/10.1063/5.0139879

Berto, A., Lavieille, P., Azzolin, M., Bortolin, S., Miscevic, M., Del Col, D.: Liquid film thickness and heat transfer measurements during downflow condensation inside a small diameter tube. Int. J. Multiph. Flow **140**, 103649 (2021) https://doi.org/10.1016/j.ijmultiphaseflow.2021.103649

Zhang, Y., Jia, L., Dang, C., Qi, Z.: Measurements of the liquid film thickness for annular flow during flow condensation in a circular tube. Int. J. Heat and Mass Transfer **187**, 122552 (2022) https://doi.org/10.1016/j.ijheatmasstransfer.2022.122552

Baptistella, V.E.C., Moreira, T.A., Ribatski, G.: Liquid-film thickness during flow boiling of pure hydrocarbons and their mixtures. Exp. Therm. Fluid Sci. **144**, 110877 (2023) https://doi.org/10.1016/j.expthermflusci.2023.110877

Fujisawa, N., Komatsu, M., Yamagata, T.: Experimental study on erosion initiation via liquid droplet impingement on smooth and rough walls. Wear **452**, 203316 (2020) https://doi.org/10.1016/j.wear.2020.203316

Khan, M.S., Sasikumar, C.: A water droplet erosion-induced fatigue crack propagation and failure in x20cr13 martensitic stainless-steel turbines working at low pressure. Eng. Fail. Anal. **139**, 106491 (2022) https://doi.org/10.1016/j.engfailanal.2022.106491

Azzopardi, B.J.: Drops in annular two-phase flow. Int. J. Multiph. Flow **23**(7), 1–53 (1997) https://doi.org/10.1016/S0301-9322(97)90087-2

Schubring, D., Shedd, T.A., Hurlburt, E.T.: Studying disturbance waves in vertical annular flow with high-speed video. Int. J. Multiph. Flow **36**(5), 385–396 (2010) https://doi.org/10.1016/j.ijmultiphaseflow.2010.01.003

An, J.S., Cherdantsev, A.V., Zadrazil, I., Markides, C.N.: Study of disturbance wave development in downwards annular flows with a moving frame-of-reference brightness-based laser-induced fluorescence method. Exp. Fluids **61**, 1–6 (2020) https://doi.org/10.1007/s00348-020-03001-w

Demekhin, E.A., Kalaidin, E.N., Kalliadasis, S., Vlaskin, S.Y.: Three-dimensional localized coherent structures of surface turbulence. i. scenarios of two-dimensional–three-dimensional transition. Phys. Fluids **19**(11) (2007) https://doi.org/10.1063/1.2793148

Bhat, F.A., Samanta, A.: Linear stability analysis of a surfactant-laden shear-imposed falling film. Phys. Fluids **31**(5) (2019) https://doi.org/10.1063/1.5093745

Kharlamov, S.M., Guzanov, V.V., Bobylev, A.V., Alekseenko, S.V., Markovich, D.M.: The transition from two-dimensional to three-dimensional waves in falling liquid films: Wave patterns and transverse redistribution of local flow rates. Phys. Fluids **27**(11) (2015) https://doi.org/10.1063/1.4935958

Bender, A., Stroh, A., Frohnapfel, B., Stephan, P., Gambaryan-Roisman, T.: Combined direct numerical simulation and long-wave simulation of a liquid film sheared by a turbulent gas flow in a channel. Phys. Fluids **31**(2) (2019) https://doi.org/10.1063/1.5064423

Aliseda, A., Heindel, T.J.: X-ray flow visualization in multiphase flows. Annual Review of Fluid Mechanics **53**(1), 543–567 (2021) https://doi.org/10.1146/annurev-fluid-010719-060201

Dupont, J., Mignot, G., Prasser, H.-M.: Two-dimensional mapping of falling water film thickness with near-infrared attenuation. Experiments in Fluids **56**, 1–16 (2015) https://doi.org/10.1007/s00348-015-1955-1

Zhao, Z., Wang, B., Wang, J., Fang, L., Li, X., Wang, F., Zhao, N.: Liquid film characteristics measurement based on nir in gas–liquid vertical annular upward flow. Meas. Sci. Technol. **33**(6), 065014 (2022) https://doi.org/10.1088/1361-6501/ac57ed

Al-Aufi, Y.A., Hewakandamby, B.N., Dimitrakis, G., Holmes, M., Hasan, A., Watson, N.J.: Thin film thickness measurements in two phase annular flows using ultrasonic pulse echo techniques. Flow Meas. Instrum. **66**, 67–78 (2019) https://doi.org/10.1016/j.flowmeasinst.2019.02.008

Skjæraasen, O., Kesana, N.R.: X-ray measurements of thin liquid films in gas–liquid pipe flow. Int. J. Multiph. Flow **131**, 103391 (2020) https://doi.org/10.1016/j.ijmultiphaseflow.2020.103391

Mizushima, Y.: Newly developed method for liquid thin film thickness measurement using optical fiber–based reflective probe. Nucl. Technol. **209**(12), 1886–1897 (2023) https://doi.org/10.1080/00295450.2023.2229998

Farias, P.S.C., Martins, F.J.W.A., Sampaio, L.E.B., Serfaty, R., Azevedo, L.F.A.: Liquid film characterization in horizontal, annular, two-phase, gas–liquid flow using time-resolved laser-induced fluorescence. Exp. Fluids **52**, 633–645 (2012) https://doi.org/10.1007/s00348-011-1084-4

Alekseenko, S., Cherdantsev, A., Cherdantsev, M., Isaenkov, S., Kharlamov, S., Markovich, D.: Application of a high-speed laser-induced fluorescence technique for studying the three-dimensional structure of annular gas–liquid flow. Exp. Fluids **53**, 77–89 (2012) https://doi.org/10.1007/s00348-011-1200-5

Charogiannis, A., An, J.S., Markides, C.N.: A simultaneous planar laser-induced fluorescence, particle image velocimetry and particle tracking velocimetry technique for the investigation of thin liquid-film flows. Exp. Therm. Fluid Sci. **68**, 516–536 (2015) https://doi.org/10.1016/j.expthermflusci.2015.06.008

Markides, C.N., Mathie, R., Charogiannis, A.: An experimental study of spatiotemporally resolved heat transfer in thin liquid-film flows falling over an inclined heated foil. Int. J. Heat Mass Transf. **93**, 872–888 (2016) https://doi.org/10.1016/j.ijheatmasstransfer.2015.10.062

Charogiannis, A., Denner, F., Wachem, B.G., Kalliadasis, S., Markides, C.N.: Detailed hydrodynamic characterization of harmonically excited falling-film flows: A combined experimental and computational study. Phys. Rev. Fluid **2**(1), 014002 (2017) https://doi.org/10.1103/PhysRevFluids.2.014002

Yan, B., Sun, Y., Sun, M., Wu, G., Gong, C., Wan, M., Tian, Y., Li, Q., Chen, S., Zhu, J.: Simultaneous visualization of instantaneous unburnt and preheating zones in turbulent premixed flames under transverse acoustic excitations. Physics of Fluids **34**(9) (2022) https://doi.org/10.1063/5.0105751

Yan, B., Sun, Y., Sun, M., Li, F., Wu, G., Wan, M., Tian, Y., Li, Q., Chen, S., Zhu, J.: Investigation of dynamic mixedness characteristics of a transverse acoustically excited turbulent jet by high-repetition-rate acetone tracer planar laser-induced fluorescence technique. Aerospace Science and Technology **136**, 108238 (2023) https://doi.org/10.1016/j.ast.2023.108238

Yan, B., Sun, M., Tang, T., Li, Y., Wang, L., Yang, X., Li, Q., Tian, Y., Chen, S., Zhu, J.: Flameholding characteristics of a circular scramjet combustor with an asymmetric supersonic inflow. Proceedings of the Combustion Institute **40**(1-4), 105306 (2024) https://doi.org/10.1016/j.proci.2024.105306

Cherdantsev, A.V., An, J.S., Charogiannis, A., Markides, C.N.: Simultaneous application of two laser-induced fluorescence approaches for film thickness measurements in annular gas-liquid flows. Int. J. Multiph. Flow **119**, 237–258 (2019) https://doi.org/10.1016/j.ijmultiphaseflow.2019.07.013

Chang, S., Yang, Y., Shi, Q., Qi, H.: Experimental study of shear-driven water film with brightness-based laser-induced fluorescence technique. Int. J. Multiph. Flow **166**, 104514 (2023) https://doi.org/10.1016/j.ijmultiphaseflow.2023.104514

Cherdantsev, A.V., Hann, D.B., Azzopardi, B.J.: Study of gas-sheared liquid film in horizontal rectangular duct using high-speed lif technique: Three-dimensional wavy structure and its relation to liquid entrainment. Int. J. Multiph. Flow **67**, 52–64 (2014) https://doi.org/10.1016/j.ijmultiphaseflow.2014.08.003

Ross, D., Gaitan, M., Locascio, L.E.: Temperature measurement in microfluidic systems using a temperature-dependent fluorescent dye. Anal. Chem. **73**(17), 4117–4123 (2001) https://doi.org/10.1021/ac010370l

Häber, T., Gebretsadik, M., Bockhorn, H., Zarzalis, N.: The effect of total reflection in plif imaging of annular thin films. Int. J. Multiph. Flow **76**, 64–72 (2015) https://doi.org/10.1016/j.ijmultiphaseflow.2015.06.009

Zadrazil, I., Matar, O.K., Markides, C.N.: An experimental characterization of downwards gas–liquid annular flow by laser-induced fluorescence: Flow regimes and film statistics. Int. J. Multiph. Flow **60**, 87–102 (2014) https://doi.org/10.1016/j.ijmultiphaseflow.2013.11.008

Xue, T., Zhang, T., Li, Z.: A method to suppress the effect of total reflection on plif imaging in annular flow. IEEE Transactions on Instrumentation and Measurement **71**, 1–8 (2022) https://doi.org/10.1109/TIM.2022.3167775

Xue, T., Li, H., Zhang, T.: Imaging and investigation with plif40 for improved film thickness measurements in annular flow. Experimental Thermal and Fluid Science **150**, 111032 (2024) https://doi.org/10.1016/j.expthermflusci.2023.111032

Rivera, Y., Bidon, M., Muñoz-Cobo, J.-L., Berna, C., Escrivá, A.: A comparative analysis of conductance probes and high-speed camera measurements for interfacial behavior in annular air–water flow. Sensors **23**(20), 8617 (2023) https://doi.org/10.3390/s23208617

Rivera, Y., Bascou, D., Blanco, D., Álvarez-Piñeiro, L., Berna, C., Muñoz-Cobo, J.-L., Escrivá, A.: Comparison of refractive index matching techniques and plif40 measurements in annular flow. Sensors **24**(7), 2317 (2024) https://doi.org/10.3390/s24072317

Jiang, M., Wang, Z., Chen, B.: Experimental investigation of film thickness in wastewater airlift pumps by an image processing method. Water **16**(14), 2010 (2024) https://doi.org/10.3390/w16142010

Charogiannis, A., An, J.S., Voulgaropoulos, V., Markides, C.N.: Structured planar laser-induced fluorescence (s-plif) for the accurate identification of interfaces in multiphase flows. Int. J. Multiph. Flow **118**, 193–204 (2019) https://doi.org/10.1016/j.ijmultiphaseflow.2019.06.002

Voulgaropoulos, V., Patapas, A., Lecompte, S., Charogiannis, A., Matar, O.K., De Paepe, M., Markides, C.N.: Simultaneous laser-induced fluorescence and capacitance probe measurement of downwards annular gas-liquid flows. International Journal of Multiphase Flow **142**, 103665 (2021) https://doi.org/10.1016/j.ijmultiphaseflow.2021.103665

Alekseenko, S., Nakoryakov, V.: Instability of a liquid film moving under the effect of gravity and gas flow. International journal of heat and mass transfer **38**(11), 2127–2134 (1995)

Nusselt, W.: Die oberflachenkondensation des wasserdamphes. VDI-Zs **60**, 541 (1916)

Inoue, C., Maeda, I.: On the droplet entrainment from gas-sheared liquid film. Phys. Fluids **33**(1) (2021) https://doi.org/10.1063/5.0038399

Inoue, T., Inoue, C., Fujii, G., Daimon, Y.: Evaporation of three-dimensional wavy liquid film entrained by turbulent gas flow. AIAA J. **60**(6), 3805–3812 (2022) https://doi.org/10.2514/1.J061381

Nikuradse, J.: Gesetzmäßigkeiten der turbulenten strömung in glatten rohren (nachtrag). Forschung auf dem Gebiet des Ingenieurwesens A **4**(1), 44–44 (1933)

Moody, L.F.: Friction factors for pipe flow. Transactions of the American Society of Mechanical Engineers **66**(8), 671–678 (1944)

Schlichting, H., Gersten, K.: Boundary-layer Theory. Springer, Berlin (2016)

Rayleigh: On the stability or instability of certain fluid motions (iii.). Proceedings of the London Mathematical Society **1**(1), 5–12 (1895)

Villermaux, E.: On the role of viscosity in shear instabilities. Phys. Fluids **10**(2), 368–373 (1998) https://doi.org/10.1063/1.869529

Dimotakis, P.E.: Two-dimensional shear-layer entrainment. AIAA J. **24**(11), 1791–1796 (1986) https://doi.org/10.2514/3.9525

Born, M., Wolf, E.: Principles of Optics: Electromagnetic Theory of Propagation, Interference and Diffraction of Light, 6th edn. Elsevier, Oxford (2013)

Shinan, C., Weidong, Y., Mengjie, S., Mengyao, L., Qiyu, S.: Investigation on wavy characteristics of shear-driven water film using the planar laser induced fluorescence method. Int. J. Multiph. Flow **118**, 242–253 (2019) https://doi.org/10.1016/j.ijmultiphaseflow.2019.04.016